NWP SAF

Satellite Application Facility for Numerical Weather Prediction

Associate Scientist Mission Report

Document NWPSAF-MO-VS-027

Version 3.0

14 September 2005

Implementation Plan for a NRT global ASCAT soil moisture product for NWP

Part 3: Azimuthal Anisotropy of Scatterometer Measurements over Land

Z Bartalis

Institute of Photogrammetry and Remote Sensing, Vienna University of Technology, Austria.

EUMETSAT Met Office ECMWF KNMI METEO FRANCE Toujours un temps d'avance

ASCAT Soil Moisture Report Series No. 3

Azimuthal Anisotropy of Scatterometer Measurements over Land

VIENNA UNIVERSITY OF TECHNOLOGY
INSTITUTE OF PHOTOGRAMMETRY AND REMOTE SENSING

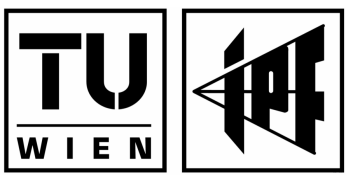

2005 Sep 14

Status:	Issue 3.0
Authors:	IPF TU Wien (ZB)
Circulation:	IPF, NWP SAF
Amendments:	

Issue	***Date***	***Details***	***Editor***
Issue 1.0	2005 May 10	Initial Document.	ZB
Issue 2.0	2005 Sep 5	First Revision	ZB
Issue 3.0	2005 Sep 14	Second Revision, after comments by Stephen English, MetOffice	ZB

If further corrections are required please contact Zoltan Bartalis. (zb@ipf.tuwien.ac.at).

Abstract

Studies of the earth's land surface involving scatterometers are becoming an important application field of microwave remote sensing. Similarly to scatterometer observations of ocean waves, the σ^0 response of land surfaces depends on both the incidence *and* azimuth angle under which the observations are made. One of the areas of interest in which scatterometry has proven useful is the retrieval of global soil moisture parameters from scatterometer data. In order to refine the obtained soil moisture products, it is necessary to account for azimuthal modulation effects of the backscattered signal. In the present study, we localize some of the regions affected by strong azimuthal signal dependency when observed with the ERS Scatterometer (ESCAT) and the SeaWinds scatterometer on Quikscat (QSCAT). We then discuss the physical reasons for the azimuthal effects, which are usually related to special small-scale topographic features. We also propose and evaluate different methods for normalizing both the QSCAT and ESCAT backscattering coefficient with respect of observation azimuth angle. A first normalising method involved using the SRTM digital elevation model and did not yield satisfactory results, due to the coarse spatial resolution of the data when compared to the microwave signal wavelength. The second normalising method was based on using historical data to determine expected values of backscatter at various azimuth angles. This method produced good results, particularly when enough historical scatterometer data was available.

The present study was funded by the *geoland* project (http://www.gmes-geoland.info) and the NWP SAF (Numerical Weather Prediction Satellite Application Facility, http://www.metoffice.com/research/interproj/nwpsaf).

Contents

1 Introduction

A scatterometer is an active microwave instrument that sends electromagnetic pulses to the surface of the earth and measures the signal scattered back in its direction, described by the normalised radar backscattering cross section or backscattering coefficient (σ^0). Quantitatively σ^0 is governed by the radar equation, which describes the relationship between the characteristics of the radar, the target and the received signal. The backscattering coefficient changes in function of the observed surface properties, most importantly dielectric properties, vegetation and roughness. In addition, it usually varies with both the incidence angle of the look direction (usually denoted θ) *and* the azimuth (horizontal) angle, usually denoted φ, between the projection of the look direction onto the observed surface and some reference direction (usually pointing north).

The primary application field of scatterometers is the retrieval of ocean near-surface wind speed and direction by measuring the backscatter from ocean waves. In addition, scatterometers have been found to be useful in an ever increasing number of studies of the earth's land and ice surfaces (Liu 2002). One of the research ambitions has been the evaluation of soil moisture based on scatterometer observations. Advances in this field in the last decade have made it possible to set up a processing chain for soil moisture retrieval at the Institute of Photogrammetry and Remote Sensing (IPF) at Vienna University of Technology (TU Wien), based on the method developed by Wagner et al. (1999). The method is based on long-term time series of ERS Scatterometer (ESCAT) data using a change detection algorithm tailored to the sensor characteristics. The algorithm exploits the multiple viewing capabilities of the sensor in order to separate soil moisture and vegetation effects. In the forthcoming text we will refer to this algorithm as the TU Wien-model.

Due to the primary aim of the ESCAT instrument (ocean wind retrieval), the instrument design is such that it permits observations of a target surface under a range of incident angles as well as under three different azimuth angles (six if both ascending and descending passes are considered), using three different antennae (see Chapter 2). The TU Wien-model is based primarily on the incidence angle dependency of σ^0 and how this dependency evolves over time. One of the first steps in the TU Wien-model is disregarding σ^0 triplet measurements in which the fore beam backscatter is too different from the aft one, by using

simple thresholding (discussed below). Although this reduces the variability of the backscatter (anisotropy) due to the different observation azimuth, substantial azimuthal effects are still observed in the time series over many geographical regions. The periodic nature of this noise-like signal variability indicates a close relationship with the satellite orbit and instrument geometry. A normalisation of the observed azimuthal modulation effects would in many cases yield substantial improvements in the accuracy of the soil moisture estimation algorithm. Currently preparations are underway to transfer the existent ESCAT soil moisture retrieval algorithms to the upcoming Advanced Scatterometer (ASCAT) scatterometer, scheduled for launch in December 2005 onboard the first of three meteorological operational (METOP) platforms, which constitute the space segment of the European Organisation for the Exploitation of Meteorological Satellites (EUMETSAT) Polar System (EPS). The ASCAT scatterometer will be similar to ESCAT, with significantly improved coverage and enhanced spatial resolution (Figa-Saldaña et al. 2002). The TU Wien-model is in principle directly applicable to ASCAT data (Bartalis et al. 2004). Better understanding and reduction of azimuthal anisotropy effects in ESCAT data will therefore benefit soil moisture retrieval from both sensors.

In the next chapter we describe the instrument geometry with associated measurement gridding for both the ESCAT and the SeaWinds onboard Quikscat (QSCAT) scatterometers. Due to its special rotating antenna design, the QSCAT scatterometer is better suited for studies of the azimuthal dependency and has for this reason been included in this study. QSCAT data will provide the base for the physical interpretation of the anisotropy presented in Chapter 3. In Chapter 4 we will discuss several ways to normalise σ^0 with respect to the azimuth angle, using first a digital elevation model, then a statistical approach. As we will see, attempting to model the QSCAT backscatter azimuthal patterns using today's most versatile, globally available digital elevation model (SRTM) yields no satisfactory results, hinting at the smaller, wavelength-comparable scale at which strong anisotropies can arise. On the other hand, a statistical normalisation based on the availability of long-term historical ESCAT data produces significant improvements, the extent of many of the problematic regions being strongly reduced. Chapter 5 presents a short conclusion of the study.

2 The ESCAT and QSCAT Data

2.1 The ESCAT Instrument

An ESCAT scatterometer has been mounted on each of ESA's ERS-1 and ERS-2 platforms (ESA 1992). ERS-1 acquired data between August 1991 and May 1996 and ERS-2 between March 1996 and January 2001, when due to a gyroscope failure all instruments onboard ERS-2 were temporarily switched off. Presently the instruments still acquire uncalibrated data (not included in this study). The nominal ground resolution of the data is coarse (approximately 50 km). Nevertheless, the instrument achieves daily global coverage of up to about 41%. In some regions (Europe, North America, etc.), the coverage is substantially reduced during at least one of the ascending or descending passes, due to simultaneous operation of the ERS SAR (Synthetic Aperture Radar) instrument, with which ESCAT shares operation time.

The ESCAT instrument consists of three antennae producing three beams looking 45° forward, sideways (90°), and 45° backward with respect to the satellite's motion direction along the orbit (see Fig. 5–1 *a*). The measurements from each beam consist of 19 so-called nodes spaced 25 km apart. As the satellite beams sweep along the earth surface yielding an approximately 500 km wide swath, each node produces its own σ^0 measurement, integrated over an area around 50 km in diameter. The three measurements originating in the three beams during the same satellite overpass are called triplets. This configuration results in the fact that for the cases of fore- and aft beams, the incidence angle of the node measurements range from 25° (innermost nodes, no. 0) to 57° (outermost nodes, no. 18). Similarly, the incidence angles for the mid-beam nodes range from 18° (node 0) to 45.5° (node 18). Table 5–1 shows the incidence angle ranges used in this study to separate the nodes into bins. The scatterometer operating frequency is 5.3 GHz (C-band), where vertical transmit and receive (VV) polarization is used. The estimated radiometric stability is better than 0.22 dB (Frison and Mougin 1996).

The ERS satellite orbit is sun-synchronous, with inclination $i = 98.52°$ (retrograde motion, opposed to the direction of the earth rotation). For each location on the surface of the earth, the scatterometer's three beams will illuminate the surface of the earth at a total of

six azimuthal angles (three for each ascending- and descending orbits), as illustrated in Figure 5–2. The values of the six azimuthal angles depend only on the location latitude λ. If not provided with the raw data, they can be calculated using Clairaut's formula (Williams 2005), valid for any point along any great circle on a spherical earth:

$$\sin\Phi\cos\lambda = constant\,, \tag{2–1}$$

where Φ is the clockwise angle between the local meridian and the direction of the motion (the so-called true course). The boundary conditions $\Phi = 270^{\circ}$ for $\lambda = 180^{\circ}–i$ or $\lambda = i - 180^{\circ}$ (in the case of ascending or descending track respectively) yield

$$\Phi_{a} = 360^{\circ} + \frac{\arcsin(90^{\circ}–i)}{\cos\lambda} \tag{2–2}$$

as the true course for any λ on the ascending track and

$$\Phi_{d} = 180^{\circ} - \frac{\arcsin(90^{\circ}–i)}{\cos\lambda} \tag{2–3}$$

as the true course for any λ on the descending track. The six azimuth angles corresponding to the six beam positions are thus given by

$$\begin{aligned} &\varphi_1 = \Phi_a + 45^{\circ}\,; \quad \varphi_2 = \Phi_a + 90^{\circ}\,; \quad \varphi_3 = \Phi_a + 135^{\circ}\,; \\ &\varphi_4 = \Phi_d + 45^{\circ}\,; \quad \varphi_5 = \Phi_d + 90^{\circ}\,; \quad \varphi_6 = \Phi_d + 135^{\circ}. \end{aligned} \tag{2–4}$$

2.2 The QSCAT Instrument

The QSCAT scatterometer was built by the Jet Propulsion Laboratory (JPL) and was launched in September 1999 onboard the Quikscat satellite into an orbit similar to that of ERS. Compared to the "fan-beam" configuration of ESCAT though, QSCAT was a novel "pencil-beam" design: rather than using fixed antennae, two radar beams are projected on the earth surface using a rotating parabolic dish (Spencer et al. 1997; Wu et al. 1994). The operating frequency is 13.4 GHz (Ku-band). As the satellite moves along its orbit, the two beams describe a double helix-shaped swath pattern (see Figure 5–1 *b*). The inner beam has horizontal (HH) polarization at 46° incidence angle, while the outer beam is vertically polarized (VV) at 54° incidence angle. The two-way 3-dB footprint size for the inner beam is approximately 24×31 km and for the outer beam 26×36 km.

Despite differences from ESCAT in terms of radar frequency, polarization and incidence angles, the capability of measuring backscatter at practically any azimuth angle make QSCAT a valuable tool in understanding azimuthal σ^0 signatures.

2.3 The Predefined Grid Systems

In order to organise backscatter time series, σ^0 measurements must be "binned" into so-called grid points which are defined as fixed points on the surface of the globe at regular intervals. Starting with the Equator, the grid points are placed on latitude circles spaced at 27.5 km distance in the case of ESCAT and 10 km in the case of QSCAT. Within each latitude circle, grid points are equally spaced also in the west-east direction, again at 27.5 and 10 km intervals for ESCAT and QSCAT respectively, starting in the eastern direction at the 0^o meridian for ESCAT and the 180^o meridian for QSCAT. A sampling window similar in size and shape to the footprint of the sensor is used in the allocation of σ^0 measurements to a grid point. All ESCAT σ^0 measurements observed within a 27.5 km radius (12.5 km for QSCAT) from the grid point are allocated to that point. The region inside which measurements allocated to a grid point originate will be called a grid area. A more detailed description of the gridding system is presented in Kidd et al. (2003).

3 Azimuthal Anisotropy over Land

3.1 State of the Art

There is relatively little material dealing with azimuthal anisotropy of either ESCAT or QSCAT σ^0 measurements, or at any wavelength, for that matter. The azimuth- and time-invariant radar response of homogenous, isotropic, large-area targets like the Amazonian rainforest or the Siberian plains has been used for calibration of both ESCAT (Long and Skouson 1996) and QSCAT (Zec et al. 2000) measurements. Especially in the case of ESCAT where measurements at different azimuth angles are acquired by different antennae, the precise inter-beam calibration is critical, since bias in antenna responses could be falsely interpreted as azimuthal anisotropy. The sources cited above suggest variability of the ESCAT signal over rainforest of about 0.15 dB. The corresponding value for QSCAT has been evaluated to 0.10 dB. These values include azimuthal modulation and are indicative of the actual radiometric resolution of the instruments.

So far studies of backscatter azimuthal anisotropy have been focusing on either ice masses or sandy desert areas. In one of the first studies, Remy et al. (1992) have observed correlation between the directional anisotropy of NASA's Seasat scatterometer signal (Ku-band) and wind-induced surface microrelief (so-called *sastrugi*) orientation over Antarctic ice sheets. Azimuthal effects were present even without oriented surface scatterers if the ice sheets featured significant overall slopes. Similar observations have been made by Young et al. (1996) using ESCAT data. Early (1998) observed azimuthal modulation of the ESCAT measurements of 1 dB or less over sea ice regions and developed methods for correcting (normalising) the data. A similar study by Remund et al. (1997) indicated sea ice anisotropy of less than 0.6 dB in Ku-band scatterometer data. Long and Drinkwater (2000) compared azimuth variation in σ^0 measurements from the NASA scatterometer (NSCAT, Ku-band), ESCAT and the Special Sensor Microwave Imager (SSMI) over Antarctica, finding again correlation with the surface slope and small-scale roughness. They also applied fitting of second-order Fourier series to the $\sigma^0(\varphi)$ periodic function, thus modelling the azimuthal backscatter behaviour.

Similar fitting of harmonic functions was performed by Stephen and Long (2002) over desert areas in North Africa and the Arabian Peninsula. In both QSCAT and ESCAT data they observed high azimuthal modulation amplitudes over the sand dune deserts (so-called *ergs*), as had been reported earlier also by Wismann et al. (1993) and Frison and Mougin (1996). The extent of the ergs was in concordance with the large isophase areas observed in the azimuthal modulation. In another Saharo-Arabian sand desert study (Stephen and Long 2003), the same authors model ESCAT and NSCAT backscatter variation with both θ and φ as the resultant of surface scattering, subsurface volume scattering and subsurface bedrock scattering. Relatively consistent results between models and observations were achieved. A more theoretical approach towards modelling scattering from Saharan sand masses the influence of wind is given in Stephen and Long (2004) and Stephen and Long (2005), where sand dunes are modelled as sets of tilted rough facets onto which ripples are superimposed. In another sand dune study Bateson and Woodhouse (2004) derive wind ripple orientation from ESCAT data and compare it with prevailing wind direction at selected sites in Niger.

3.2 Physical Considerations

Scatterometer measurements are usually accompanied by information about the *nominal* incidence and azimuth angle at which backscatter is measured. In most cases, the backscattering coefficient decreases rapidly with increasing incidence angle. However, the topography of the land surface within the satellite footprint can alter the actual backscatter so that at various azimuthal look angles it differs significantly from the theoretical backscatter that we would expect from a footprint imaged under a spatially uniform and constant incidence angle. We have grouped the different topographical mechanisms that azimuthally modulate the backscatter in the following categories:

1. *Sloping surface backscattering targets with predominant slope orientation.* As suggested by Fig. 5–3, although the σ^0 measurement is made at the nominal incidence angle θ, due to the local slope the angle determining the backscatter is actually the local incidence angle θ_L. If the size of the sloping targets is comparable to or larger than the footprint size, a plot of the backscatter versus azimuth angle will have one peak and one trough, or one lobe in a polar plot (Fig. 5–4 a). This should be the case of azimuthal effects from mountain ranges and the sloping marginal areas of Antarctic or Greenlandic ice sheets. If the footprint covers several sloping and spatially aligned targets that are still larger than the wavelength, backscatter will be amplified if the satellite is facing the slopes (Fig. 5–4 b,c). This is anticipated to be the case of aligned crop fields and sand dunes.

2. *Corner reflectors with predominant orientation.* In this case the slopes of the aligned scattering targets within the footprint become so steep that a double or multiple "bounce" interaction of the radar signal becomes possible. Backscatter in certain viewing directions from a few point-like targets becomes so high that it can affect the response over the entire footprint (Fig. 5–4 d). This could be the case of urban areas laid out along a rectangular grid.

3. *Resonant Bragg scattering.* Scatterometers emit coherent electromagnetic radiation, i.e. the different wavefronts of the emitted spectrum are 'in phase'. When targets with predominant orientation are comparable in size with the radar wavelength of the scatterometer (usually for lightly rough surfaces with root mean square height variation up to about one eighth of the radar wavelength), the backscattered waves will be subjected to constructive interference at certain incidence angles (Fig 5–5). The Bragg equation defines the relationship between the wavelength of the orientational surface patterns (ripples) λ_R, the wavelength of the electromagnetic radiation λ, the incidence angle θ and the azimuthal difference between the incoming radar beam and the longitudinal orientation of the ripple crests and troughs (Ulaby et al. 1982):

$$\lambda_R = \frac{n\lambda}{2\sin\theta} \cdot \sin\varphi\,, \tag{3–1}$$

where n is the order number. In microwave applications, normally the lowest order number $n = 1$ applies (Henderson and Lewis 1998). For QSCAT, the first-order λ_R equals 1.56 cm for the inner beam and 1.38 cm for the outer beam. For ESCAT, $\lambda_R = 9.16$ cm for the lowest incidence angle and $\lambda_R = 3.37$ cm for the highest incidence angle. Bragg scattering governs backscatter from wind-induced ripples (so-called capillary- and short gravity waves) on the ocean surface (Long et al. 1996). It seems very likely that reflections from surface ripples on sand dunes also reinforce each other coherently.

It is very important to note that azimuthal modulation is due to one *or more* of the enumerated surface backscattering mechanisms, as well as due to contributions from volume scattering inside the upper layers of the reflecting media. In case of dry sand desert areas the signal usually penetrates deep enough to reach the underlying bedrock, in which case any bedrock surface topography could contribute to the overall azimuthal modulation.

3.3 The Magnitude of the Azimuthal Anisotropy

Within the current implementation of the TU Wien-model, the absolute value of the fore-aft beam difference in σ^0 for each triplet is considered to be a measure for the azimuthal anisotropy of ESCAT measurements:

$$\delta_a = \left|\varphi_1 - \varphi_2\right| \qquad \delta_d = \left|\varphi_3 - \varphi_6\right| \tag{3–2}$$

where the indices a and d denote ascending and descending satellite passes, respectively.

Fig. 5–6 shows the absolute value of the mean value of these differences, calculated for all available data between 1991 and 2001. As discussed earlier, the six acquisition azimuth angles $\varphi_{1,2\ldots6}$ depend on the latitude and thus the difference δ shown in Fig. 5–6 is not spatially normalised. Nevertheless, the azimuthal difference between the fore and aft beams for any given triplet is constant (90°) and thus δ gives us a good idea about the geographical distribution of the "problematic" areas. In addition, even though the fore-aft difference might not capture the maximal backscatter difference that a certain grid area might exhibit, in practice for any given location on the surface of the earth, the azimuth angles at which both the ESCAT and ASCAT scatterometers acquire measurements will always be limited to the six (twelve for ASCAT) discussed above. Any azimuthal normalisation must therefore only be concerned with effects observed at these angles.

As shown in Table 5–2, the mean value of δ is approximately 0.14 dB for both δ_a and δ_d, with around 45% of the land area exhibiting δ's larger than 0.1 dB. As expected, very low values are registered over the tropical forest. Of the regions displaying higher δ we can distinguish both mountainous regions (the Himalayan plateaus, the Andes, the Alps, etc) and non-mountainous areas (north-eastern China, northern Kazakhstan, North American prairies, etc). Areas with extremely large δ up to several dB are found in desert areas (Sahara, Arabian Peninsula, Kara-Kum, Taklamakan, etc) and on the Greenlandic ice sheet.

Though δ does highlight areas with high anisotropy, in itself it does not reveal how serious the anisotropy is with respect to the soil moisture retrieval. A good indicator of this would be the quotient between δ and the sensitivity to soil moisture, both measured in decibels. The sensitivity to soil moisture is defined as the difference between the typical backscatter for saturated (wet) conditions (100% degree of saturation) and the typical backscatter for dry conditions (0% degree of saturation). Fig. 5–7 shows this quotient expressed in percent. Over some mountainous regions in Europe, Canada, South America and most of central-south Asia the values range up to 30 percent, while many of the steppe and prairie regions are affected by up to 10%. These are thus the degrees of improvement we can expect by normalising the backscatter with respect to azimuth angle.

It is interesting to notice the relatively high values over tropical forests in Fig. 5–7 are actually not due to high δ, but because of very low sensitivity over these areas (vegetation effects are too strong). A notable exception is the high topographic slopes of the central mountain range on New Guinea island, where also an increased azimuthal anisotropy is observed (see Fig. 5–6).

3.4 Examples of Observed Anisotropy

In this chapter we present backscatter measurements from four regions covering 5×5° latitude and longitude, characterised by one or more predominant periodic surface orientations as described in Chapter 3.2. As mentioned earlier, we use QSCAT measurements because of the instrument's superior azimuthal sampling capabilities. For convenience, we consider only the measurements originating in the inner beam of the instrument. To describe the asymmetric σ^0 response for each grid point, we consider all available measurements from the period 1999-2004 which we plot against their acquisition φ. By taking so many measurements (in the order of 10,000 for each grid point) evenly distributed in time, we make sure that any influence of seasonal variability in terms of soil moisture, vegetation and roughness is averaged out.

The $\sigma^0(\varphi)$ relationship, being a periodic function, is then modelled as a fifth-order harmonic function given by:

$$\sigma^0(\varphi) = C + \sum_{i=1}^{5} A_i \cos(i\,\varphi - \varphi_i)\,, \qquad (3\text{–}3)$$

where C is the mean σ^0, A_i is the amplitude of the i-th order harmonic and φ_i is the phase of the i-th order harmonic. The order of the harmonic that predominates over all others will yield the characteristic shape of the different polar diagrams in Fig. 5–4, the number of lobes being equal to the predominant harmonic order. The angular offset of the lobes is governed by the phase of the harmonic with the equivalent order.

3.4.1 First Order Harmonic Predominance

Figure 5–8 a. shows the distribution of the QSCAT σ^0 measurements as a function of azimuth angle for the QSCAT grid point located on the south-western flanks of the Pyrenees in Spain, at 42.792°N and 0.694°W. The aforementioned harmonic function is fitted to the data using least-squares minimisation. The obtained curve is also shown in Figure 5–8 b. in a polar diagram. Due to the large scale slope dominating the satellite footprint, the predominant harmonic order is clearly the first one. The azimuth angle of the axis of the main lobe, being around 190° clockwise from north, agrees well with the W-NW – E-SE orientation of the main slopes of the mountain range in this area. The difference between the highest and lowest value of the modelled harmonic curve is approximately 1 dB, a significant anisotropy given that the mean backscatter for this point is around –10 dB. The spatial distribution of the first order harmonic amplitude A_1 for the region in question is presented in Figure 5–8 c., also displaying the approximate extent of the grid area of the considered QSCAT grid point (approximately 55 km in diameter). Apart from some residual effects from the

fourth order harmonic over urban areas (see Chapter 3.4.3 below), A_1 is highest over the Pyrenees, as expected.

3.4.2 Second Order Harmonic Predominance

Unexpectedly high azimuthal dependence can be observed in both ESCAT and QSCAT data over agricultural areas in north-eastern China. Figure 5–9 a. and b. show the backscatter azimuthal behaviour for the grid point at 47.643°N and 125.435°E. Although the data has a relatively large variability due to seasonal bias from the vegetation cycle, the second-order harmonic is dominating the anisotropy. This point is within a region with high second order harmonic amplitude A_2 in the left half of Fig. 5–9 c. The north-eastern half of the area is dominated by the heavily forested range of the Lesser Khingan Mountains, not displaying any significant azimuthal modulation. A hint to the origins of the remarkable double-lobes in the western part of the area can be found in the LANDSAT scene in Fig. 5–9 d.: the land in this part of the Chinese Heilongjiang province was subjected to vast reclamation projects instituted under the government in the 1950s and 1960s. Winter wheat, millet, sorghum and soy beans are the most common crops in the area, being cultivated in a highly mechanised manner. Long parallel strings of villages are laid out along east-western lines, the narrow fields stretching between the villages in the north-south direction. The narrow fields are an indication that the ploughing and sowing direction is almost without exception made in the north-south direction, leaving crop rows with faces sloping towards the east and west. Although the crop rows are not visible at the resolution of the optical image, the polar diagram of the backscatter azimuthal dependence reveals clearly their orientation. Consistent areas with east-west double lobes have also been observed over the prairies of the Canadian Saskatchewan province, where the crop fields are not even long and narrow, but seem to be perfectly square.

3.4.3 Fourth Order Harmonic and Corner Reflector Predominance

Very high azimuthal modulation can also be observed in certain areas in northern Italy as well as over large urban areas in general. In Fig. 5–10 the grid point at 45.487°N and 12.004°E has been chosen, situated in the middle of the plains between the Brenta and Piave rivers. This region is also characterised by agriculture along well-planned patterns (vineyards, etc). However, the very regular shape of the backscatter-azimuth dependency in which the fourth order harmonic has the by far largest influence, as well as the very large A_4 amplitude indicate the presence of backscattering according to the corner-reflector principle. Indeed, the LANDSAT image in Fig. 5–10 d. reveals a rectangular network of roads, probably laid out along the directions of earlier drainage channels. This in turn implies that a large number of vertical features (building walls, fences, etc) in the urban areas along the roads

form right angles, giving very strong radar response at 90° azimuthal interval.

Another noticeable aspect is how well large urban areas like Munich or Prague can be discerned in the amplitude image. This suggests that point-like corner reflectors present in cities and industrial areas "azimuthally contaminate" backscatter response from large areas around them.

3.4.4 Scattering from Predominantly Oriented Targets at Multiple-Scales

The most significant azimuthal modulation, with magnitudes of 5-10 dB occurs over the vast ergs found in the desert areas in Africa, the Arabian Peninsula and Central Asia. Wind erosion in large sand areas is similar in many ways to how wind interacts with the ocean surface, how water transports sediments on a river bed or how snow drifts (Bagnold 1941). On a general level, all these processes involve the transport of solid particles by fluids, thereby generating a very complex system of topographic features at various scales. The study of the interaction of electromagnetic waves in the microwave range with such sand features is complicated by response not only from the surface layers of the matter but also from the deeper layers in form of volume scattering.

The sand dunes in the dry interior of continents are usually not stabilised by vegetation and tend to migrate under the driving influence of prevailing winds. Depending on the prevailing wind directions and the availability of sand, moving dunes can be classified into two main kinds, longitudinal and transverse (Bagnold 1941). Longitudinal dunes form usually in areas with two prevailing wind directions 180° apart, in which case they align themselves parallel to the two upwind directions. Longitudinal dunes can be very long and straight and they usually have two slip-sides with very similar slope. When the sand availability decreases, or the prevailing wind comes exclusively from one direction, the dunes tend to align themselves in the crosswind direction, forming transverse dunes. In between the truly longitudinal and transversal cases dunes one can find a variety of complex dunes like the star dunes or the interrupted, half-moon shaped *barchans*.

Figure 5–11 shows the QSCAT azimuthal response in the grid point at 17.599°N and 11.065°E in the Grand Erg de Bilma sand desert in north-eastern Niger. The mean σ^0 is very low as expected, due to very dry conditions and absorption in the sand. The backscatter presents a large peak rising very sharply at around 330° as well as a smaller peak at approximately 140° (Fig. 5–11 a,b). Since in this case the modulation does not seem to be dominated by either of the harmonic orders, in Fig. 5–11 c. we chose to display the backscatter range (difference between the highest and lowest σ^0) rather than any of the harmonics. The image is dominated by two connected extensive features with very high modulation. Incidentally, in a spatial plot of the mean σ^0 (not shown), these two areas have also the lowest backscatter, which sug-

gests that the largest sand accumulations are to be found in these areas. Examining topographic maps and LANDSAT imagery like the detail shown in Fig. 5–11 f., as well as knowledge about two seasonal prevailing easterly and westerly winds in this region confirms the fact that the bright areas are mostly made up of longitudinal dunes. The spatial distribution of the azimuth angle of the highest σ^0 (the peak at 0º for the selected grid point) is plotted in Figure 5–11 d. The same azimuth values plotted as vectors and colour coded with the values from Figure 5–11 c. are shown in Figure 5–11 e. We observe several sharply delimited areas with high azimuthal consistency (isophase). The high modulation area in the close neighbourhood of the selected grid point has its peaks aligned in the north-south direction, suggesting an east-west dune orientation. However, even without angular ambiguities, in general it is not straightforward to associate azimuthal response with dune type, orientation and wind direction. One of the reasons for this and for the extreme magnitude of the modulation might lie in resonant scattering not from the dunes themselves, but rather from the ripples which usually are found on the slopes of the dunes and which do not necessarily have the same orientation as the dunes. In Chapter 4.1 we will attempt to quantify the contribution of the dunes to the azimuthal modulation.

Figure 5–11 e. also emphasises a few small areas with higher elevation, notably the ridge that cuts into the two bright areas from the north, pointing out again that azimuthal response is governed by topographic features orientation at a number of various scales.

4 Accounting for the Azimuthal Modulation

For normalising the azimuthal dependence of the backscatter measurements one could make use of empirical methods or modelling. Both approaches could be based on either the data itself and/or external datasets. It would be clearly advantage if the normalisation could be done without relying too much on other datasets than the ESCAT or ASCAT backscatter. In this chapter we first try to model the azimuthal modulation using the SRTM (Shuttle Radar Topography Mission) DEM (Digital Elevation Model), then we use the historic backscatter data do derive biases for each category of σ^0 measurements.

4.1 Modelling Azimuthal Response using the SRTM DEM

The Shuttle Radar Topography Mission obtained unprecedented high-resolution global elevation data through a specially modified radar altimeter system that flew onboard the Space Shuttle Endeavour during an 11-day mission in February 2000. In this study we used the SRTM-3 C-band product, having a spatial resolution of 3 arcseconds (approximately 90 m), with an absolute horizontal accuracy of 20 m and an absolute vertical accuracy of 16 m at 90% confidence level (JPL 2005).

The purpose of the modelling was to determine how well a digital elevation model of 90 m spatial resolution can represent topographic features governing azimuthal modulation of the backscatter, and implicitly, whether we could use such an elevation model for accounting for the anisotropies. For doing this, we extract SRTM elevation data within 27.5 km distance from each grid point to approximate the topography of the grid area. We convert the latitude/longitude SRTM elevation grid to the Albers Equal Area projection in order to give each pixel the same weight. We then derive the surface slope s and aspect a, according to the formulae

$$s = \tan^{-1}\sqrt{\left(\frac{h_{21}-h_{01}}{2x}\right)^2+\left(\frac{h_{10}-h_{12}}{2y}\right)^2} \text{ and} \tag{4–1}$$

$$a = \tan^{-1}\left(\frac{h_{21}-h_{01}}{2x}, \frac{h_{10}-h_{12}}{2y}\right), \tag{4–2}$$

here x and y are the pixel dimensions in the easting and northing directions respectively and h_{ij} are elevation values for the 3×3 pixel window M centred on the pixel h_{11} which will hold the slope and aspect values:

$$M = \begin{bmatrix} h_{00} & h_{10} & h_{20} \\ h_{01} & h_{11} & h_{21} \\ h_{02} & h_{12} & h_{22} \end{bmatrix} \tag{4–3}$$

Using the slope and aspect we determine the local incidence angle θ_L (see Fig. 5–3) for each SRTM pixel when viewed under an incidence angle equal to that of the QSCAT inner beam (46°) and an azimuth angle ranging from 0 to 360°. In this process we do not consider pixels with $\theta_L > 90°$ as this means that the pixel faces away from the sensor. We do not account for so-called shadowing effects, occurring when pixels obstruct each other's path. The resulting simulations for the Pyrenees and Niger grid points are shown in Fig. 5–12. The first three plots in each row show elevation, slope and aspect respectively. The fourth plots are histograms of the aspect value of all SRTM pixels, visualised in polar form. These give an idea of the general slope magnitude and orientation for that grid area. As expected, the histograms indicate correctly both the south-eastern slopes of the Pyrenees and the two oppositely sloping faces of the sand dunes (the peaks at multiples of 45° are artefacts due to preferential aspect directions along the rectangular pixel grid). In the last plots we simulate a 360°-tour of the grid areas at 46° incidence angle, showing the mean θ_L for all SRTM pixels at any given azimuth (blue). The standard deviation associated to this mean is also shown (red). We notice that in the case of the Pyrenees, as the sensor completes a circle around the grid area, the mean local incidence cycles from about 47.2° to 49.7° whereas the standard deviation stays high and almost unchanged (14.8°-15.4°). The less than 3° change in mean local incidence angle as well as the relatively homogenous distribution of the values (as indicated by the high standard deviation) make it unlikely that the variation in mean local incidence angle alone can account for the backscatter variation of 1 dB.

In the case of the Niger grid area, the situation speaks even more against the appropriateness of the SRTM to explain the azimuthal modulation. Although the standard deviation is much lower (more pointed distribution of θ_L), the change in mean θ_L is hardly 2°. This in itself cannot possibly imply a backscatter change of almost 8 dB and indicates again the dominant role of the small-scale sand ripples. The low change in θ_L is obvious after we notice from Figs. 5–12 f., g. that the dune interspacing is around 1 km whereas the average dune height is around 80 m. Furthermore, the polar histogram in Fig. 5–12 i. shows significantly more pixels with northern aspect, meaning that statistically the southern slopes of the dunes are steeper. In the possibility of non-resonant backscatter this in turn would mean that the backscatter should be higher when looking at the dunes from the south, which is clearly contradicted by the data. Another unexplained aspect is the certain asymmetric bias in azimuth between the two main backscatter

lobes (cf. Figs. 5–12 i. and 5–11 b.) that is noticed in many grid areas covering this type of longitudinal dunes.

In conclusion, although in the case of mountain slopes the model produced a fairly good estimation of the azimuthal modulation, the relatively high spatial resolution of the SRTM DEM is still not high enough to make the data useful for modelling azimuthal anisotropies at Ku-band radar frequencies. Especially when compared to small scale periodic ripples, the contribution of the 90 m scale topographic features can practically be neglected.

4.2 Backscatter Normalisation using Historical Data

Another azimuthal normalisation approach consists in normalising the σ^0 measurements with respect to azimuth angle, using all previously acquired data to derive statistically expected values. For doing this, it is important to keep in mind that the azimuthal anisotropy $\sigma^0(\varphi)$ can vary in time and at different incidence angles. This results directly from the definition of the backscattering coefficient as a function of incidence angle, azimuth angle and time:

$$\sigma^0 = f(\theta, \varphi, t) \tag{4–4}$$

For each grid point, the number of possible combinations of azimuth and incidence angles in the case of ESCAT is $6 \cdot 19 = 114$. Thus, ideally, if enough historical σ^0 measurements would be available for each of the 114 cases, each incoming measurement could be reliably normalised azimuthally by adding a positive or negative bias that represents the difference between the expected backscatter value for the azimuth and incidence angle in question and a backscatter value measured or derived at a reference azimuth angle. If we would like to account for any seasonal variability of the magnitude of the azimuthal anisotropy, the number of azimuth-incidence-time combinations would actually become $114 \cdot n$, where n is the number of chosen time periods a year would be divided into (e.g. 12 months). To illustrate the possible seasonal variation of the azimuthal anisotropy, Figure 5–13 shows the monthly evolution of the QSCAT backscatter vs. azimuth relationship, averaged from all available data.

Unfortunately, despite the more than nine years of ESCAT data, the lack of a statistically relevant number of σ^0 measurements for all the different aforementioned azimuth-incidence-time combinations means that a robust normalisation has to compromise in terms of one or more of the three variables. The number of annual ESCAT σ^0 measurements per year for each of the 114 azimuth-incidence combinations varies typically from around 5-30 at the Equator to around 30-65 at 70° latitude. As mentioned, these values are further diminished in a significant way by the outfall of scatterometer operation during most of the descending tracks over areas such as Europe and North America (due to

concurrent SAR operation). A refinement of the normalisation including 12 monthly periods is therefore not meaningful for large areas of interest.

A compromise along the lines of incidence angle is feasible by reducing the number of incidence angle bins. If we plot the incidence angle ranges for the 19 nodes for all three ESCAT beams (Fig. 5–14, Table 5–1), we notice that five of the mid-beam node incidence angles coincide especially well with five of the fore- and aft beam incidence angles. In "fore-mid-aft" notation the node number combinations for these five cases are 0-4-0, 3-8-3, 5-11-5, 7-14-7 and 10-18-10. The needed correction biases can be determined for these five incidence angles for each of the six azimuth angles (Fig. 5–15) and stored in a look-up table for each grid point. The magnitude of the corrections for nodes other than those present in the five combinations can then be calculated using linear interpolation/extrapolation or fitting various other functions. Figure 5–16 shows two examples of approximating the correction bias κ for all nodes from the five node combinations. In Figure 5–16 a) the κ values for the lower and higher end of the incidence angle range are equalled to the correction for node combinations 0-4-0 and 10-18-10 respectively, while the middle incidence angle range is linearly interpolated. The correction for the two extremities of the incidence angle range could alternatively be equalled to the correction for one or more of the nodes in that range. In Figure 5–16 b) the incidence angle dependence of the azimuthal anisotropy is neglected, a constant κ (the arithmetical mean of κ for the five node combinations) being used for all the nodes.

The improvements achieved using the two methods from Figure 5–16 can be seen in Figures 5–17 and 5–18, where the δ's before and after correction are compared. Additionally to the Chinese study area, a region in the Canadian prairies is shown. Interestingly, a Landsat image (not shown) of the latter, highly agricultural region does not reveal the orientation of the crop rows, most crop fields being square-shaped. The very similar azimuthal signature (second-order harmonic predominance) as in the case of the Chinese region reveals though that even here, the crop rows have a north-south predominant orientation. In Figures 5–17 and 5–18, each of the two normalisation methods has been applied on both yearly and monthly basis. We see that in all four cases, significant reduction in δ has been achieved. The monthly corrections are somewhat more effective in reducing the azimuthal effects, but also, as expected, noisier than the yearly ones.

5 Conclusions

In this study the azimuthal dependence (anisotropy) of the scatterometer backscattering coefficient σ^0 over land has been investigated. Regions with high such dependence have been localised, using a parameter denoting the magnitude of the inter-beam backscatter difference of the ESCAT scatterometer. The geometrical characteristics of different azimuthally modulating surfaces have been presented, followed by some examples of scatterometer data exhibiting anisotropies believed to be governed by these different categories of surface geometry.

An attempt to model azimuthal anisotropies using the SRTM digital elevation model has only been partially successful, due to the much coarser spatial resolution of the elevation model when compared to the radar wavelengths in question.

A possible approach for correction (normalisation) of azimuthal effects has then been described, based on the statistically expected backscatter values at different incidence angles and/or times of the year. In general significant reduction of the anisotropy was noticed after applying the normalisation procedures. Any normalisation method based on historical data should be effective enough to acceptably account for periodic variation of backscatter due to varying acquisition azimuth and at the same time robust enough to deal with the lack of historical measurements over many parts of the earth's land masses.

Bibliography

Bagnold, R. A. (1941). The Physics of Blown Sand and Desert Dunes. London, Methuen & Co.

Bartalis, Z., K. Scipal, V. Naeimi and W. Wagner (2004). Soil moisture products from C-band scatterometers: From ERS-1/2 to METOP. ENVISAT-ERS Symposium, Salzburg, Austria, 6-10 September 2004.

Bateson, L. and I. H. Woodhouse (2004). *Observations of scatterometer assymetry over sand seas and derivation of wind ripple orientation.* International Journal of Remote Sensing **25**(10): 1805-1816.

Early, D. S., (1998) A Study of the Scatterometer Image Reconstruction Algorithm and its Applications to Polar Ice Studies, dissertation at the Department of Electrical and Computer Engineering, Brigham Young University, Provo, UT

ESA (1992). *ERS-1 System.* Technical Report SP-1146. Frascati, Italy, European Space Agency.

Figa-Saldaña, J., J. J. W. Wilson, E. Attema, R. Gelsthorpe, M. R. Drinkwater and A. Stoffelen (2002). *The advanced scatterometer (ASCAT) on the meteorological operational (MetOp) platform: A follow on for European wind scatterometers.* Canadian Journal of Remote Sensing **28**(3): 404-412.

Frison, P. L. and E. Mougin (1996). *Use of ERS-1 wind scatterometer data over land surfaces.* IEEE Transactions of Geoscience and Remote Sensing **34**: 550-560.

Henderson, F. M. and A. J. Lewis (1998). Principles and Applications of Imaging Radar. New York, John Wiley & Sons.

JPL, *Shuttle Radar Topography Mission,* http://www2.jpl.nasa.gov/srtm/, accessed on 2005 Mar 10

Kidd, R. A., M. Trommler and W. Wagner (2003). The development of a processing environment for time-series analysis of SeaWinds scatterometer data. IGARSS 2003, Toulouse, France, 21-25 July 2003.

Liu, W. T. (2002). *Progress in Scatterometer Application.* Journal of Oceanography **58**: 121-136.

Long, D. G., R. S. Collyer, R. Reed and D. V. Arnold (1996). *Dependence of the Normalized Radar Cross Section of Water Waves on Bragg Wavelength-Wind Speed Sensitivity.* IEEE Transactions of Geoscience and Remote Sensing **34**(3): 656-666.

Long, D. G. and M. R. Drinkwater (2000). *Azimuth variation in microwave scatterometer and radiometer data over Antarctica.* IEEE Transactions on Geoscience and Remote Sensing **38**(4): 1857-1870.

Long, D. G. and G. B. Skouson (1996). *Calibration of spaceborne scatterometers using tropical rain forests.* IEEE Transactions on Geoscience and Remote Sensing **34**(2): 413-424.

Remund, Q. P., D. S. Early and D. G. Long (1997). *Azimuthal Modulation of Ku-Band Scatterometer Sigma-0 Over the Antarctic.* MERS Technical Report, Bringham Young University.

Remy, R., Ledroit and J. F. Minster (1992). *Katabatic Wind Intensity and Direction over Antarctica Derived from Scatterometer Data.* Geophysical Research Letters **19**: 1021-1024.

Spencer, M. W., C. Wu and D. G. Long (1997). *Tradeoffs in the design of a spaceborne scanning pencil beam scatterometer: Application to Sea-Winds.* IEEE Transactions on Geoscience and Remote Sensing **35**: 115–126.

Stephen, H. and D. G. Long (2002). *Azimuth modulation of backscatter from SeaWinds and ERS scatterometers over the Saharo-Arabian deserts.* **5**: 2808-2810.

Stephen, H. and D. G. Long (2003). *Surface statistics of the saharan ergs observed in the Sigma-0 azimuth modulation.* **3**: 1549-1551.

Stephen, H. and D. G. Long (2004). *Analysis of scatterometer observations of saharan ergs using a simple rough facet model.* Geoscience and Remote Sensing Symposium, 2004. IGARSS '04. Proceedings. **3**: 1534-1537.

Stephen, H. and D. G. Long (2005). *Microwave Backscatter Modeling of Erg Surfaces in the Sahara Desert.* IEEE Transactions of Geoscience and Remote Sensing **43**(2): 247.

Ulaby, F. T., R. K. Moore and A. K. Fung (1982). Microwave Remote Sensing: Active and Passive. Volume 2: Radar Remote Sensing and Surface Scattering and Emission Theory. Reading, Massachusetts, Addison-Wesley, Advanced Book Program.

Wagner, W., G. Lemoine and H. Rott (1999). *A method for estimating soil moisture from ERS scatterometer and soil data.* Remote Sensing of Environment **70**(2): 191-207.

Williams, E., *Aviation Formulary v1.42,* http://williams.best.vwh.net/avform.htm, accessed on 2005 Feb 14

Wismann, V., K. Boehnke and C. Schmullius (1993). Large scale radar signatures of the land surface measured by the ERS-1 scatterometer. International Geoscience and Remote Sensing Symposium, 16-19 Aug. 1993, Tokyo, Japan.

Wu, C., J. Graf, M. Freilich, D. G. Long, M. Spencer, W. Tsai, D. Lisman and C. Winn (1994). The SeaWinds scatterometer instrument. International Geoscience and Remote Sensing Symposium, Pasadena, CA, 1994 Aug 8-12.

Young, N. W., D. Hall and G. Hyland (1996). Directional anisotropy of C-band backscatter and orientation of surface microrelief in East Antarctica. First Australian ERS Symposium, Hobart, CSIRO Office of Space Science and Applications.

Zec, J., L. Jones and D. G. Long (2000). SeaWinds beam and slice balance using data over Amazonian rainforest. IGARSS 2000, Hilton Hawaiian Village, Honolulu, Hawaii, 24-28 July 2000.

Figures and Tables

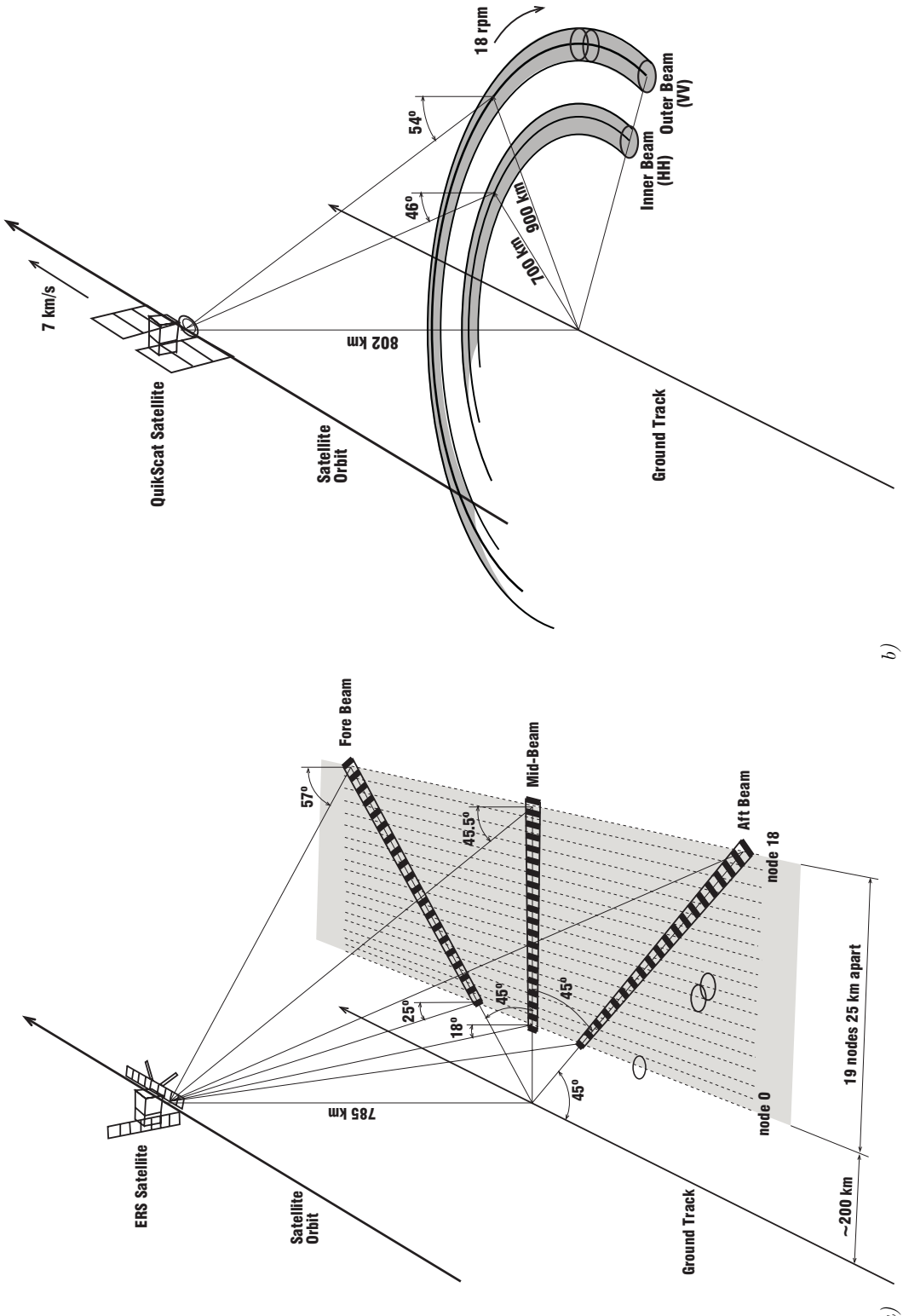

Figure 5-1.
a) The ESCAT scatterometer.
b) the QSCAT scatterometer.

Figure 5–2.

Illustration of the ascending and descending tracks and the 6 different azimuth angles under which the ESCAT scatterometer can view the surface of the earth.

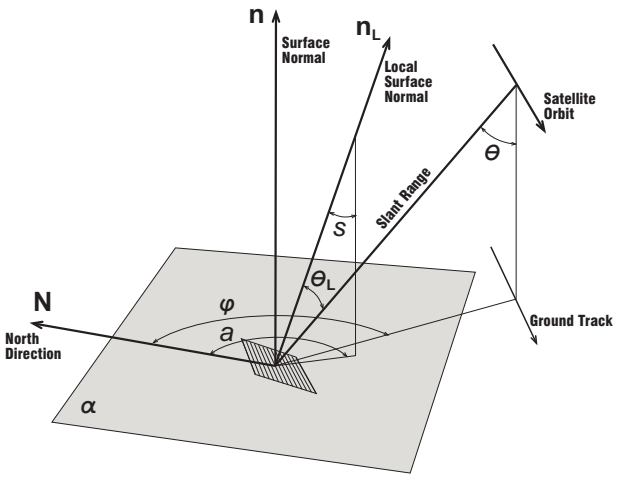

Figure 5–3.

Viewing geometry.

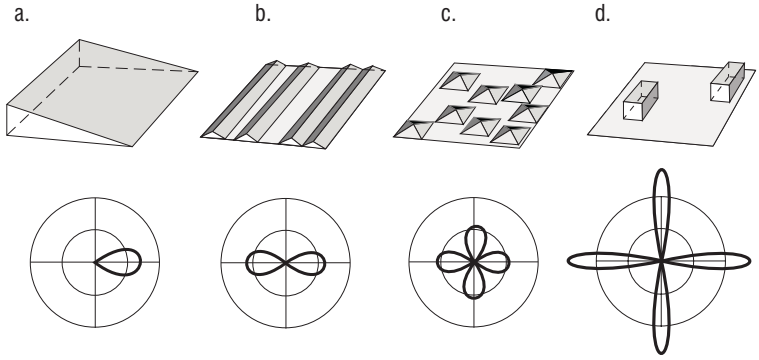

Figure 5–4.

Illustration of different sloping backscattering targets and their corresponding schematic polar plots of backscattering coefficient versus azimuth angle.

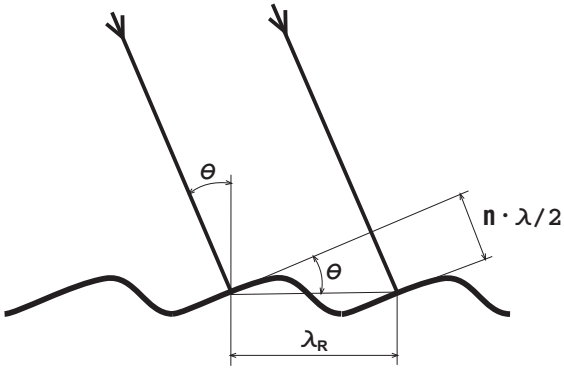

Figure 5–5.

Resonant Bragg scattering over targets with spatially isotropic surface patterns.

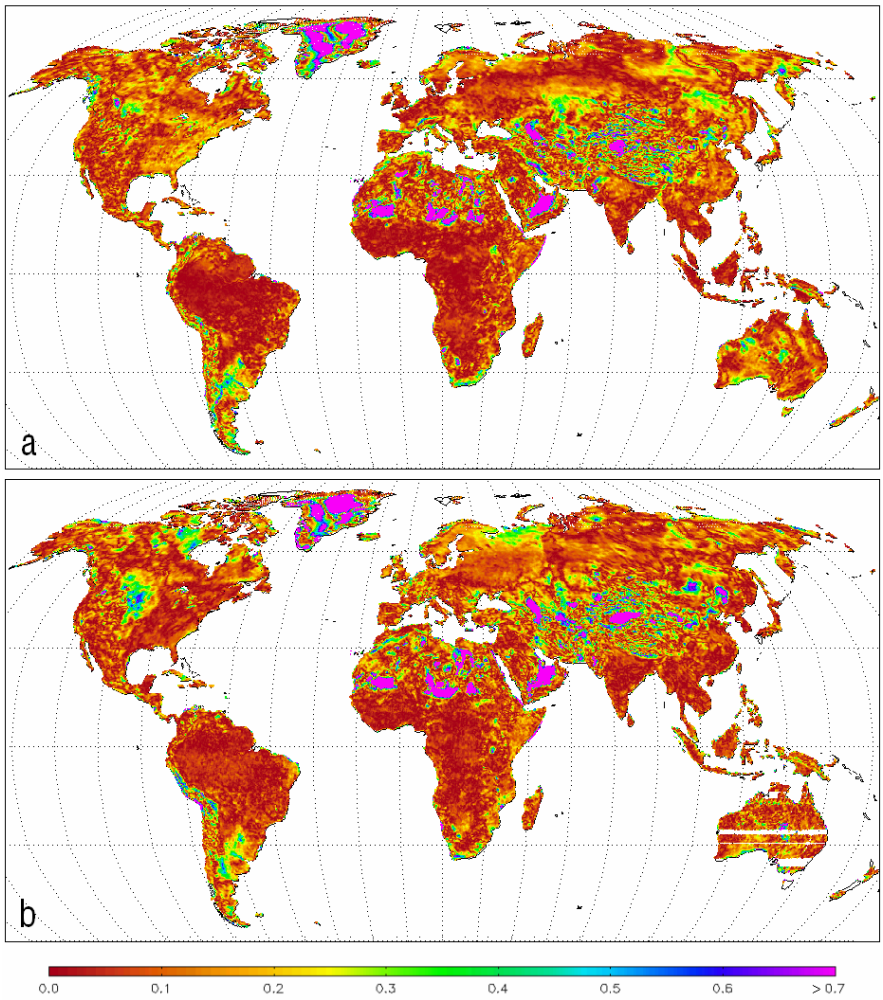

Figure 5–6.

Absolute values of the mean differences between fore and aft ESCAT backscatter (in decibels) taken triplet-wise for a) ascending tracks; b) descending tracks.
No descending track backscatter data was acquired over parts of Australia, hence the horizontal stripes.

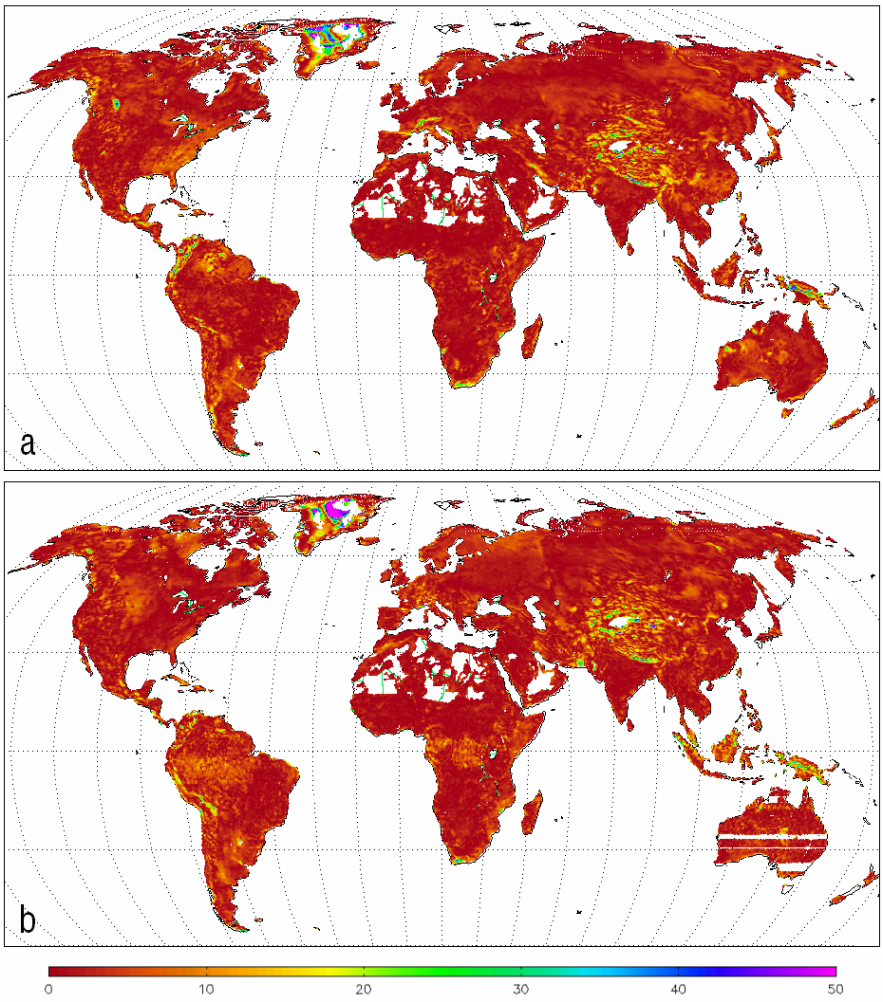

Figure 5–7.

Absolute values of the mean differences between fore and aft ESCAT backscatter taken triplet-wise, divided by the sensitivity to soil moisture for a) ascending tracks; b) descending tracks. Values are in percent.
The gaps over the large sand desert areas are due to missing sensitivity information.
No descending track backscatter data was acquired over parts of Australia, hence the horizontal stripes.

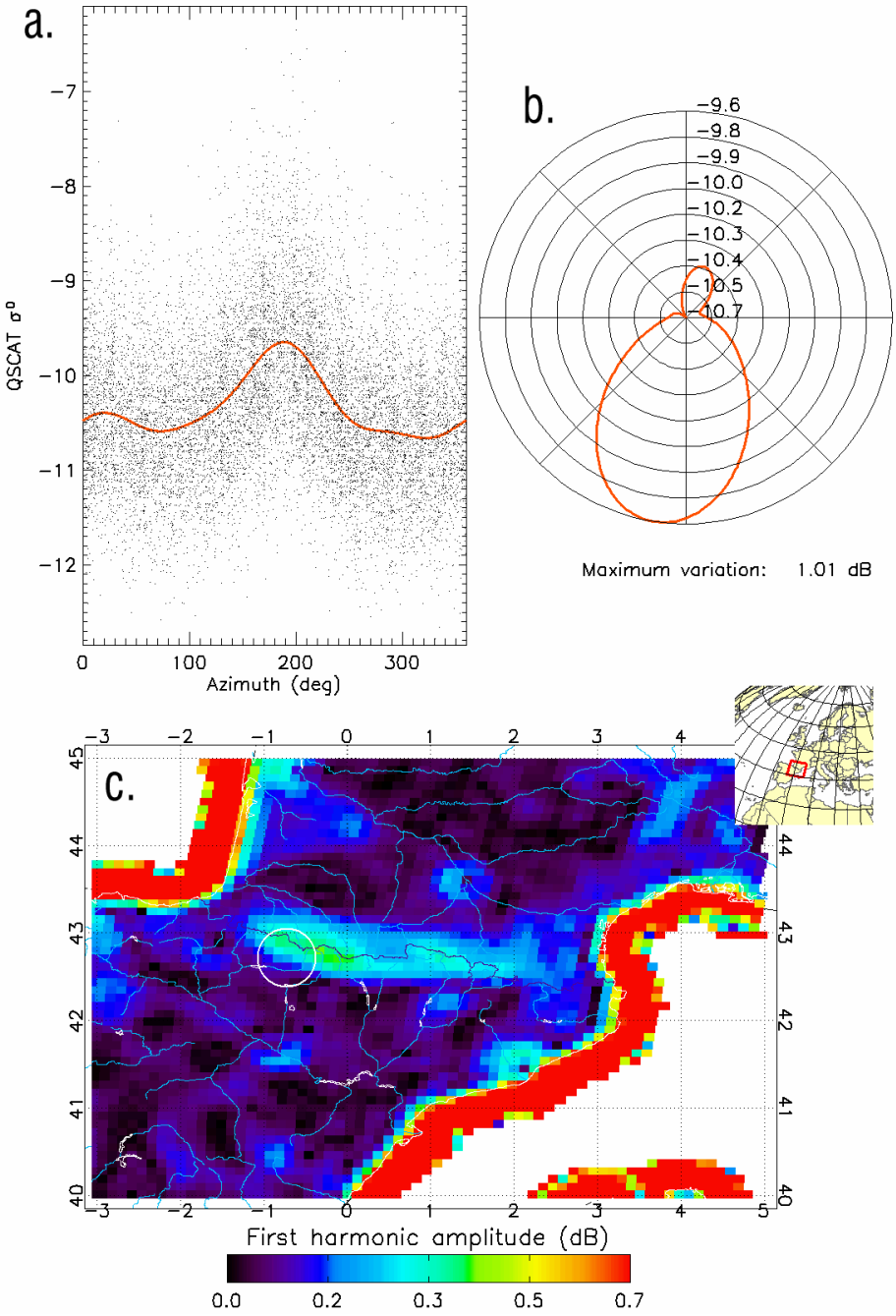

Figure 5-8.

Illustration of first order harmonic dominance over the Pyrenees in Spain.

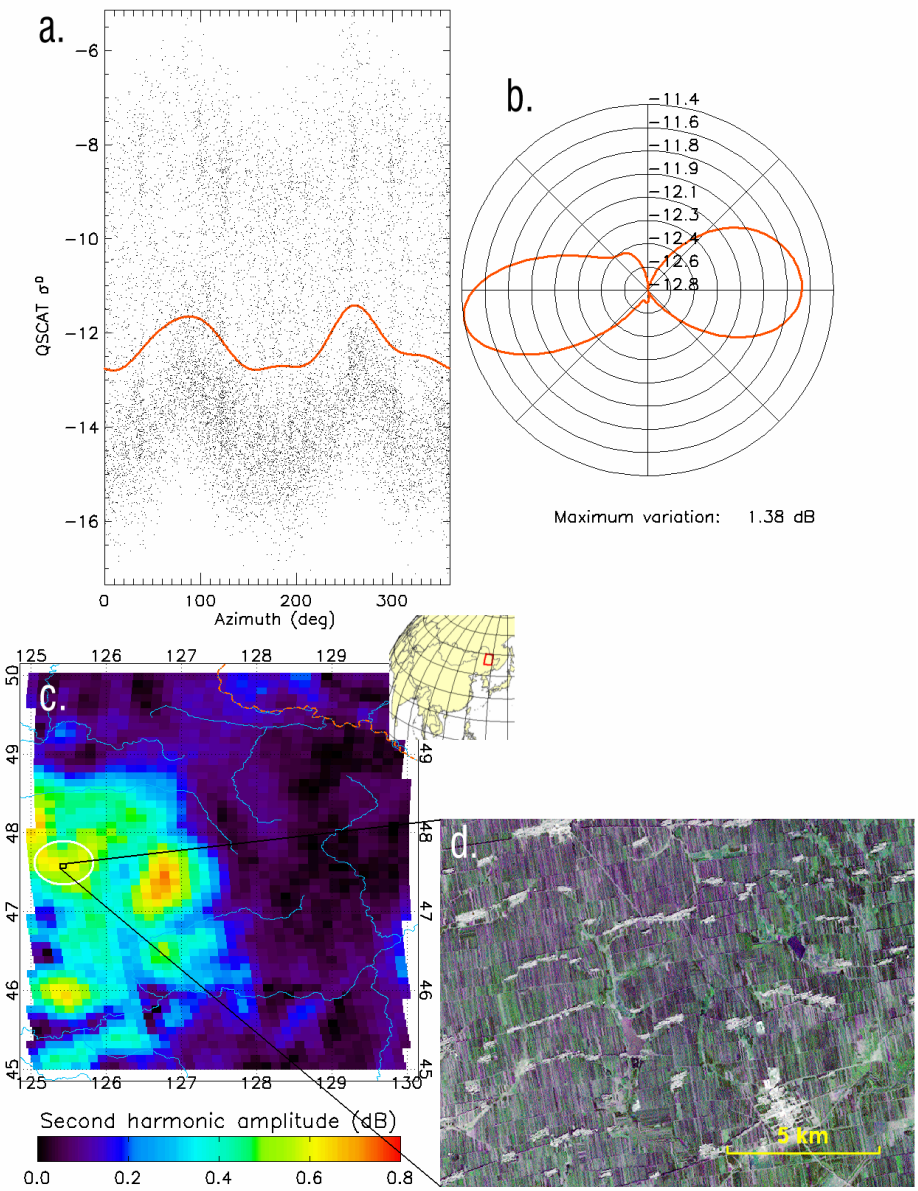

Figure 5-9.

Illustration of second order harmonic dominance in the Heilongjiang region in northeast China.

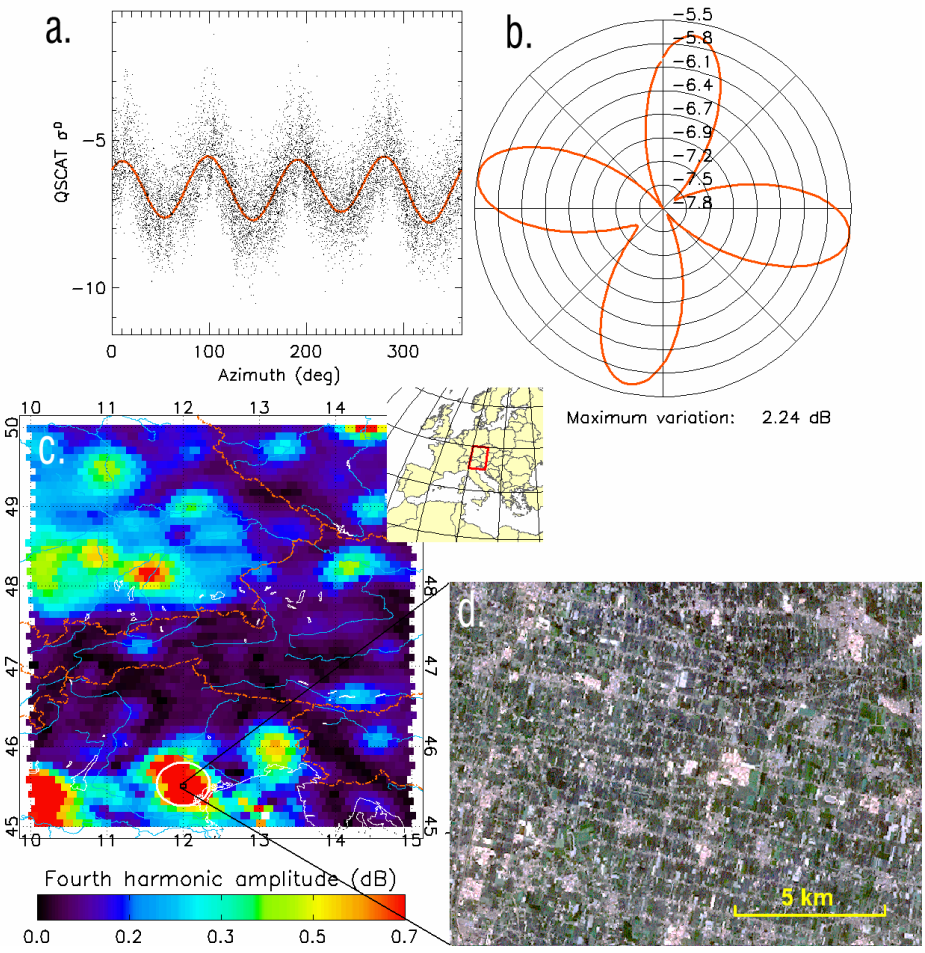

Figure 5–10.

Illustration of fourth order harmonic and corner reflector dominance in the Veneto region in northern Italy as well as the cities in Austria and southern Germany.

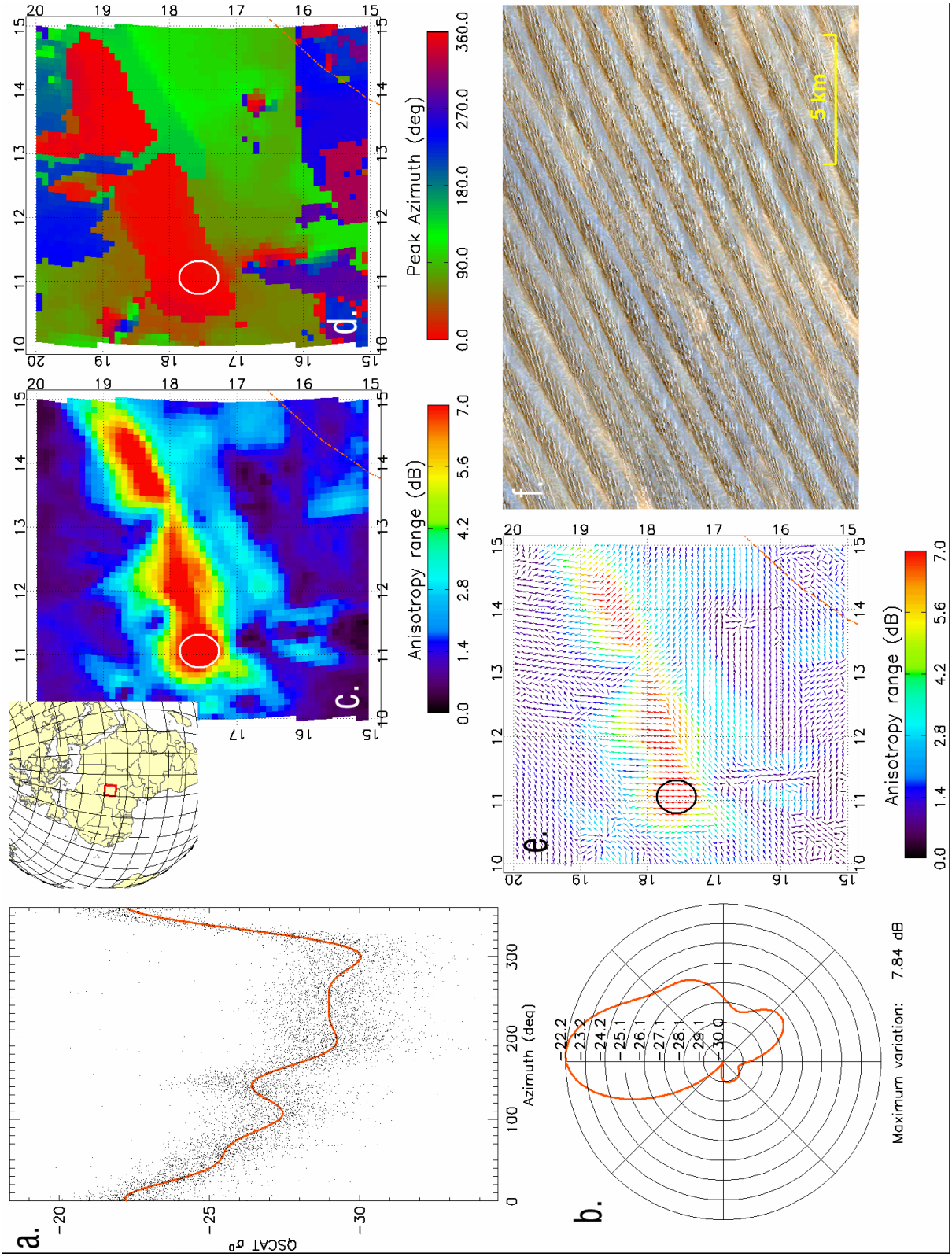

Figure 5-11.
Illustration of azimuthal modulation from sand dunes and ripples in the Grand Erg du Bilma in north-eastern Niger.

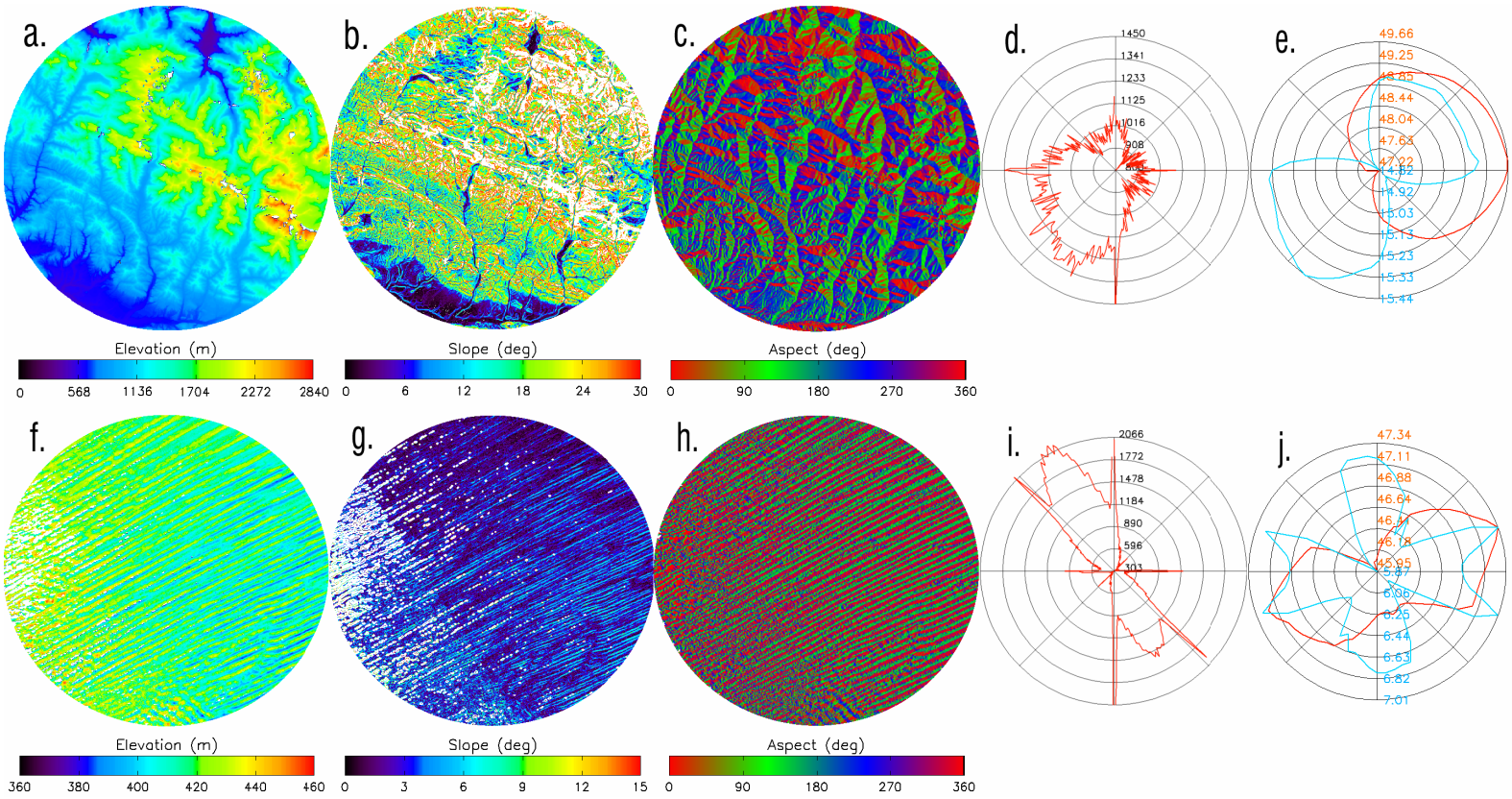

Figure 5-12.

Simulation of local incidence angle using SRTM data. Areas of 55 km in diameter approximate the QSCAT grid areas. a)-e): Pyrenees grid area (see Fig. 5–8); f)-j); Niger grid area (see Fig 5-11).
d),i): aspect polar histogram.
e), j): simulated local incidence angle mean (red, in dB) and its standard deviation (blue, in dB).

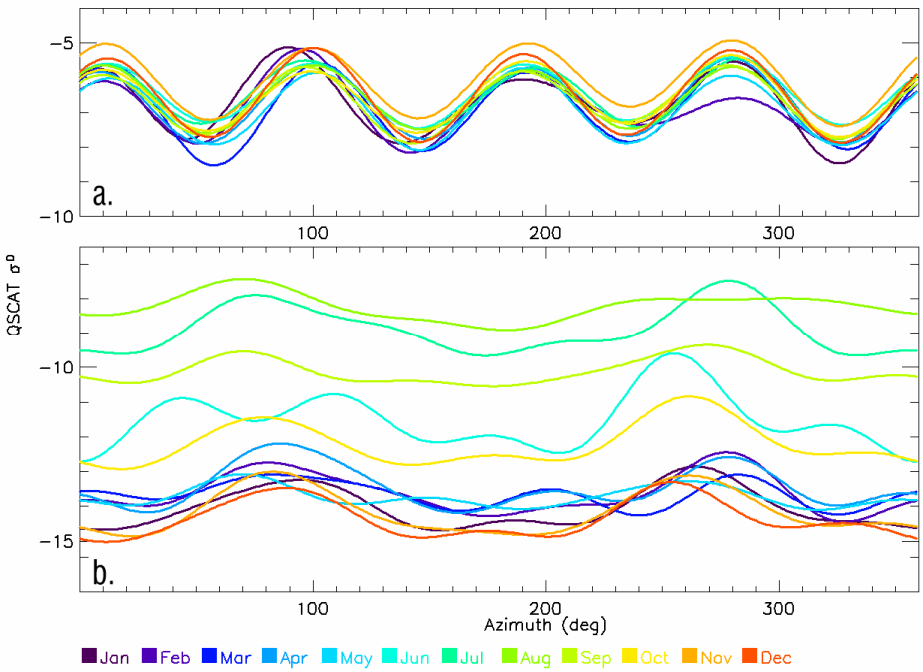

Figure 5–13.

Seasonal variability of the QSCAT azimuthal modulation for a) the Italian grid point in Fig. 5–10; b) the Chinese grid point in Fig. 5–9.

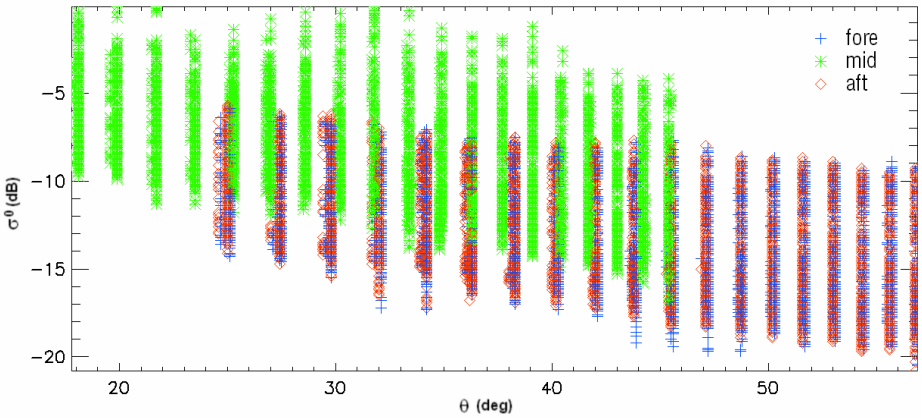

Figure 5–14.

Typical relation between backscatter and available incidence angles for fore-, mid- and aft beams, each with 19 incidence angle nodes.

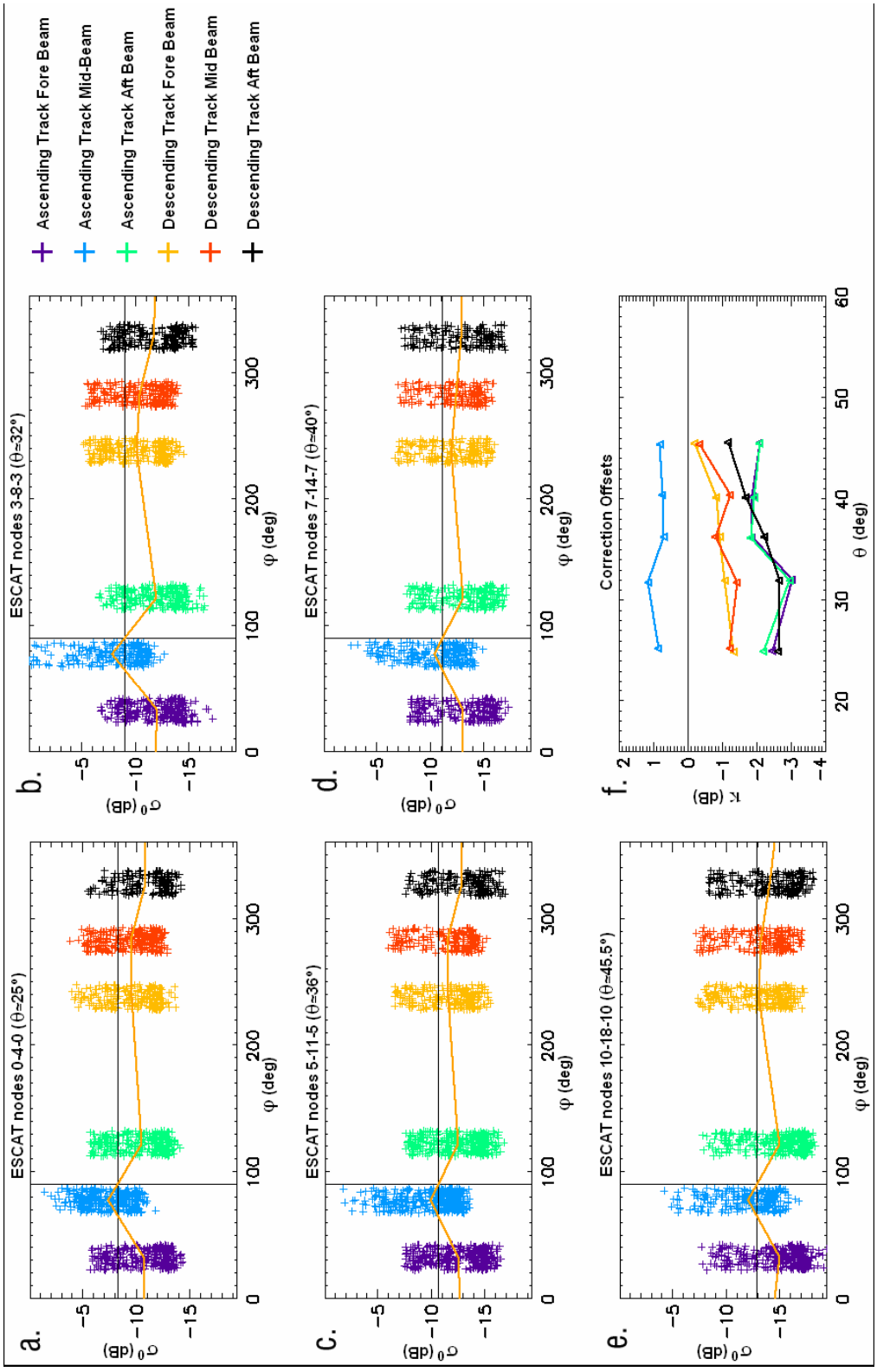

Figure 5-15.

a) – e) Example of backscatter – azimuth angle relationship for the five selected cases where the incidence angle of the fore-, mid- and aft beams coincide. The distribution of the backscatter measurements around the six possible azimuth angles was widened artificially for the sake of visibility. Also shown are the correction biases needed for normalisation with respect to 90° azimuth angle (yellow lines).

f) correction biases from a) – e) plotted against incidence angle.

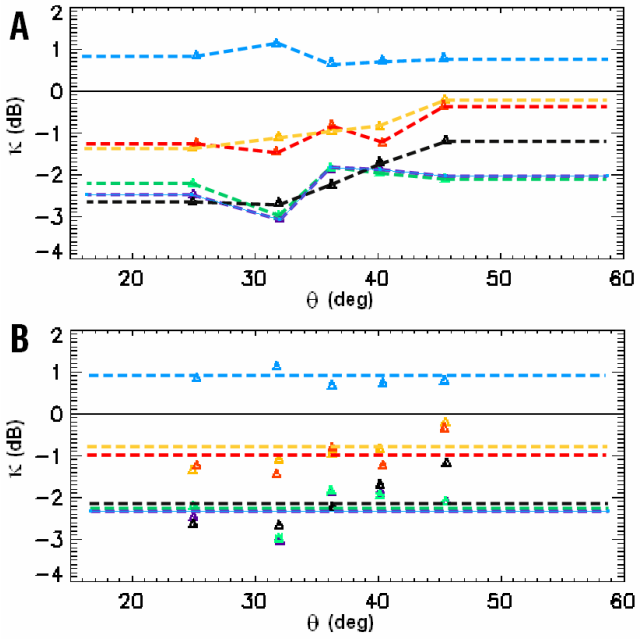

Figure 5–16.

Examples of approximating the correction bias – incidence angle relationship for each of the azimuth angles presented also in Fig. 5–15: a) linear interpolation between the five selected node combinations and constant functions outside of these; b) constant function (arithmetic mean) for all the incidence angle range.

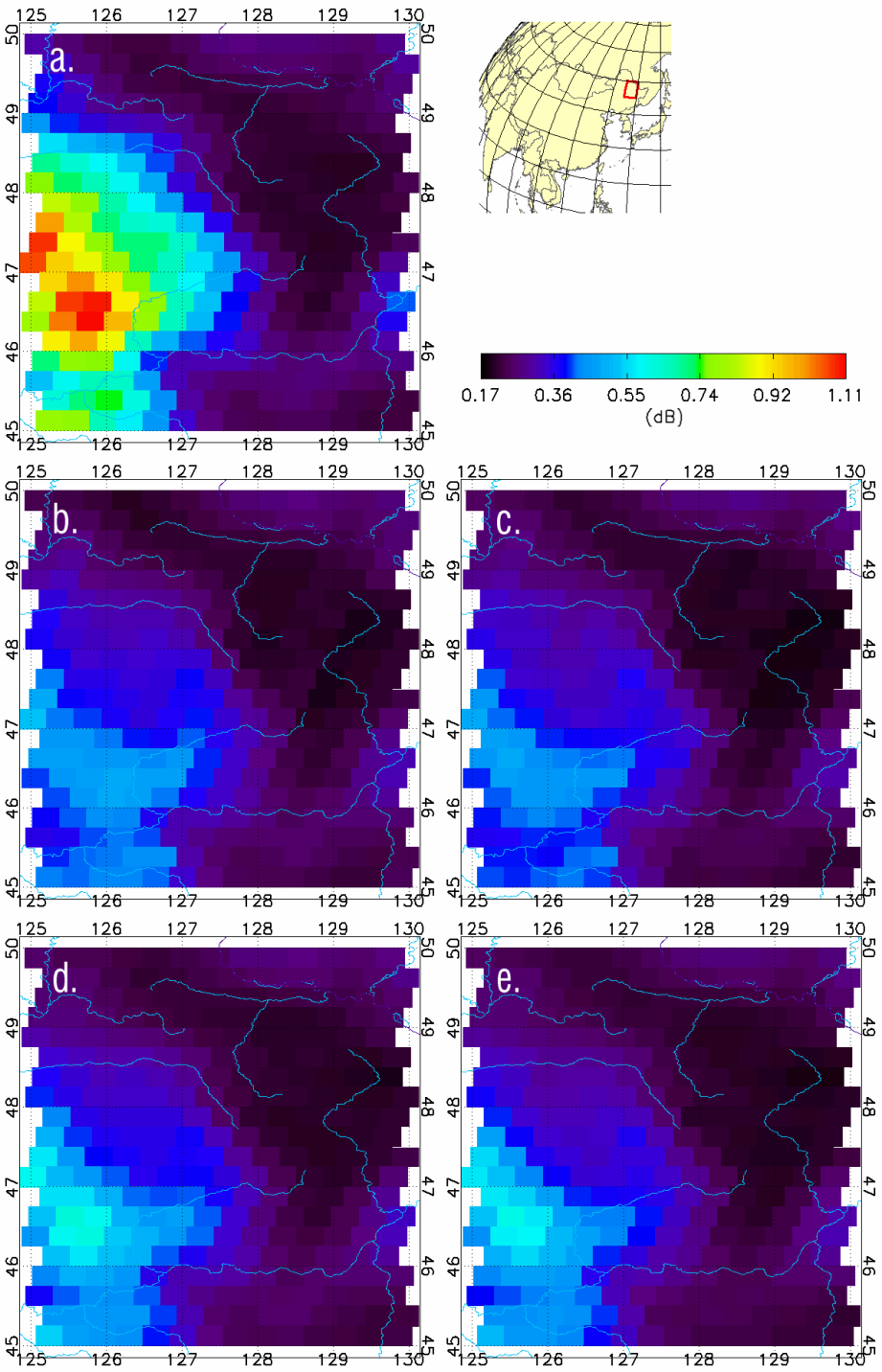

Figure 5–17.

Absolute values of the mean differences between fore and aft ESCAT backscatter (in decibels) taken triplet-wise for the descending track measurements over the Chinese study region. a) unnormalised values; b) values after normalisation with method A in Fig. 5–16, without considering seasonal dependency; c) values after normalisation with method A in Fig. 5–16, where separate normalisation was applied for the 12 months of the year; d) values after normalisation with method B in Fig. 5–16, without considering seasonal dependency; e) values after normalisation with method B in Fig. 5–16, where separate normalisation was applied for the 12 months of the year.

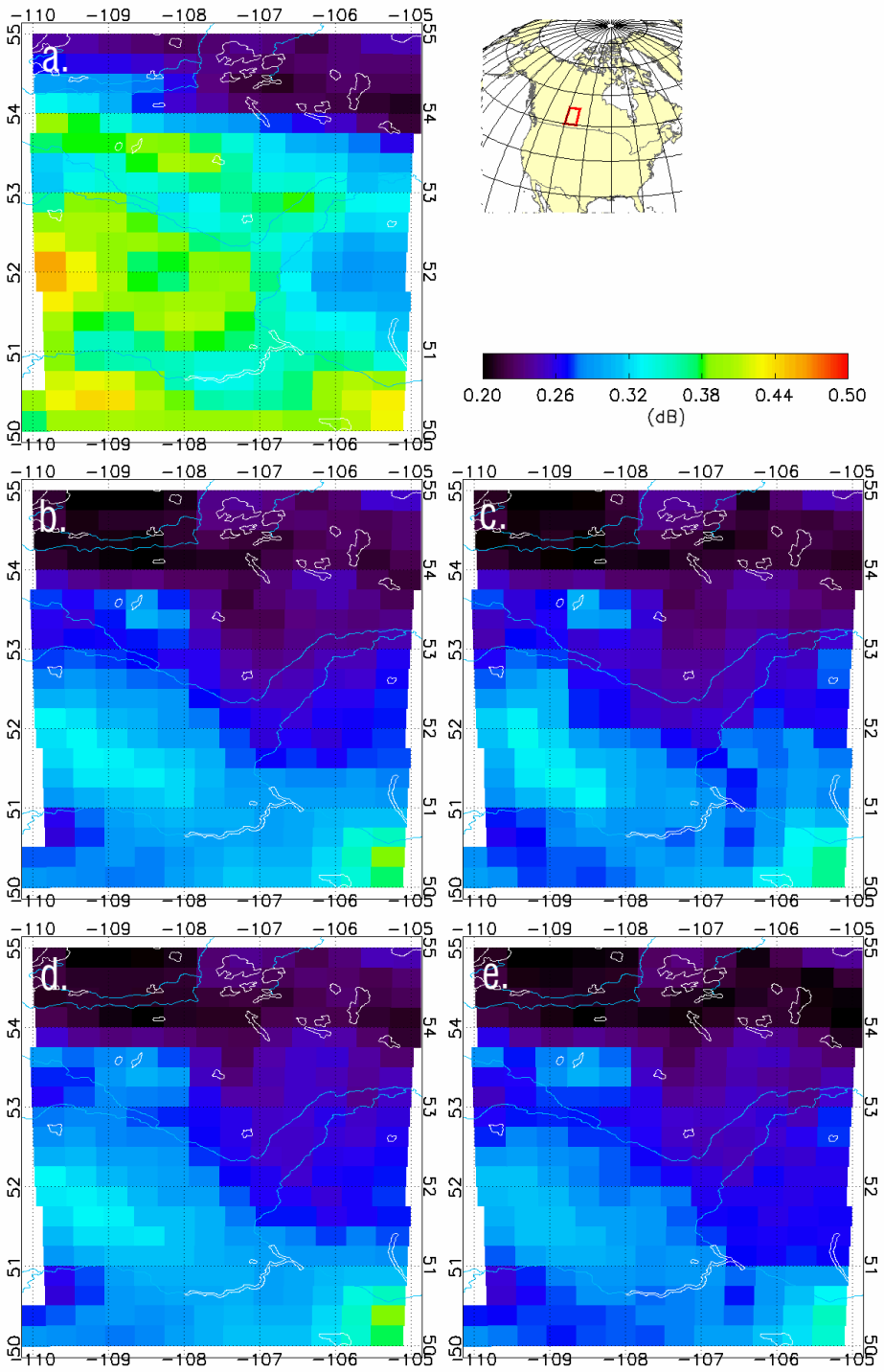

Figure 5–18.

Absolute values of the mean differences between fore and aft ESCAT backscatter (in decibels) taken triplet-wise for the ascending track measurements over a region in the Canadian prairies where azimuthal anisotropies similar to those in the Chinese region were observed. For the explanation of the different diagrams refer to the previous figure.

Node No.	Incidence Angle Bins			
	Fore/Aft Beam		Mid-Beam	
	from (deg)	to (deg)	from (deg)	to (deg)
0	23.7	26.2	17.0	19.0
1	26.2	28.6	19.0	21.0
2	28.6	30.9	21.0	22.5
3	30.9	33.0	22.5	24.3
4	33.0	35.2	24.3	26.1
5	35.2	37.3	26.1	27.8
6	37.3	39.2	27.8	29.4
7	39.2	41.2	29.4	31.0
8	41.2	43.0	31.0	32.6
9	43.0	44.8	32.6	34.2
10	44.8	46.3	34.2	35.6
11	46.3	48.0	35.6	37.0
12	48.0	49.4	37.0	38.4
13	49.4	50.9	38.4	39.8
14	50.9	52.3	39.8	41.0
15	52.3	53.8	41.0	42.3
16	53.8	55.0	42.3	43.7
17	55.0	56.3	43.7	44.9
18	56.3	57.9	44.9	46.4

Table 5–1.

Incidence angle bins for the different ESCAT nodes.

	ascending	descending
mean δ	0.137 dB	0.145 dB
percentage of δ larger than 0.1 dB	44.01 %	42.89 %
percentage of δ larger than 0.2 dB	18.07 %	18.32 %
percentage of δ larger than 0.5 dB	3.11 %	3.65 %
percentage of δ larger than 1.0 dB	1.01 %	1.27 %

Table 5–2.

The magnitude of the observed azimuthal anisotropy.